applied optics

Spectrophotometric determination of turbid optical parameters without using an integrating sphere

Xiaohui Liang,[1] Meihua Li,[1] Jun Q. Lu,[2] Chuanwei Huang,[1] Yuanming Feng,[3] Yu Sa,[3] Junhua Ding,[4] and Xin-Hua Hu[2],*

[1]Experimental Instrument Plant, AMMS, Beijing 100850, China
[2]Department of Physics, East Carolina University, Greenville, North Carolina 27858, USA
[3]Department of Biomedical Engineering, Tianjin University, Tianjin 300072, China
[4]Department of Computer Science, East Carolina University, Greenville, North Carolina 27858, USA
*Corresponding author: hux@ecu.edu

Spectrophotometric quantification of turbidity by multiple optical parameters has wide-ranging applications in material analysis and life sciences. A robust system design needs to combine hardware for precise measurement of light signals with software to accurately model measurement configuration and rapidly solve a sequence of challenging inverse problems. We have developed and validated a design approach and performed system validation based on radiative transfer theory for determination of absorption coefficient, scattering coefficient, and anisotropy factor without using an integrating sphere. Accurate and rapid determination of parameters and spectra is achieved for microsphere suspension samples by combining photodiode-based measurement of four signals with the Monte Carlo simulation and perturbation-based inverse calculations. The three parameters of microsphere suspension samples have been determined from the measured signals as functions of wavelength from 400 to 800 nm and agree with calculated results based on the Mie theory. It has been shown that the inverse problems in the cases of microsphere suspension samples are well posed with convex cost functions to yield unique solutions, and it takes about 1 min to obtain the three parameters per wavelength.   © 2016 Optical Society of America

OCIS codes: (120.6200) Spectrometers and spectroscopic instrumentation; (290.4210) Multiple scattering; (290.3200) Inverse scattering.

http://dx.doi.org/10.1364/AO.55.002079

1. INTRODUCTION

Spectrophotometers are designed to characterize a sample by determination of its optical parameters as functions of wavelength λ from measured light intensity signals. The instrument essentially solves a sequence of inverse problems at multiple λ values and has a long history of applications [1]. The current approach measures the collimated transmittance $T_c(\lambda)$ in the form of absorbance $A(\lambda)$, defined by $A = -\log(T_c)$. Using the Beer–Lambert law, an attenuation coefficient μ_t can be explicitly solved by $\mu_t(\lambda) = 2.30A(\lambda)/D$ after correction of reflection losses at index-mismatched interfaces, where D is the sample thickness and the contribution of scattered light to T_c is assumed to be negligible. The knowledge of $\mu_t(\lambda)$, however, is insufficient to accurately characterize turbid samples, since μ_t is the sum of absorption coefficient μ_a and scattering coefficient μ_s according to the radiative transfer equation (RTE) [2]. In the case of particle suspensions, one may need both coefficients to fully

characterize such materials, since $\mu_a(\lambda)$ reports the molecular composition of the suspension, while $\mu_s(\lambda)$ profiles the particulate morphology on scales close to λ. The inability of the existing spectrophotometric instrument to do so has long been noted, and various regimes have been devised to measure scattered light signals integrated over large angular cones that could be calculated or estimated quickly with a forward model [3]. Significant progress has been made over the last few decades on the study of light transport in turbid media and spectrophotometric methods for recovering parameters such as $\mu_a(\lambda)$ and $\mu_s(\lambda)$ from the measured signals [4–12]. While these results provide the underlying principles, no system designs have been developed and validated that could lead to general-use instruments comparable to existing spectrophotometers in terms of robustness on the inverse solutions and ease of use with simple sample assembly.

A practical approach to solving the inverse problems for the new spectrophotometric instruments may be best derived from

the boundary-value problems defined by the time-independent and single-energy RTE and the Fresnel equations as boundary conditions [2,13]. Within this approach, a homogeneous turbid sample is characterized by refractive index n, μ_a, μ_s, and single-scattering phase function $p(\theta, \varphi)$, where θ, φ are the polar and azimuthal angles of the scattered light direction, respectively, from the incident direction. The function $p(\theta, \varphi)$ is often approximated by an axially symmetric function $p_{HG}(\cos \theta)$ first proposed by Henyey and Greenstein, whose form of smooth angular dependence is determined by a single parameter of anisotropy factor g as the mean value of $\cos \theta$ [2]. Even with $p_{HG}(\cos \theta)$ as the phase function and known refractive index n, solving the inverse problems rapidly to determine μ_a, μ_s, and g from the measured signals is difficult, since no explicit solutions are available, and robust algorithms are needed to solve implicitly by iterations of signal calculations. Extension to instrumentation presents additional requirements such as accuracy of measured signals, tolerance to modeling errors for robust inverse solutions, ease of use, reasonable time to complete, and cost effectiveness.

The inverse problems of radiative transfer can be solved with different methods, and diffusion approximations of RTE have been actively investigated for their capability to obtain closed-form forward solutions for samples with a regular-shaped boundary. Despite numerous applications [14], diffusion models with different degrees of approximation do not provide a robust approach, because the modeling errors in light transport may become significant in samples of small to moderate single-scattering albedo $a = \mu_s/\mu_t$. Alternatively, the integro-differential RTE can be solved numerically with the discrete ordinate method or the adding-doubling method [2,5–7,10,15]. But the former needs sophisticated code development to simulate realistic geometry of sample, holder, and detectors that may frequently change due to optical designs, while the latter assumes semi-infinite parallel-plane geometry to calculate hemispherically integrated reflectance and transmittance.

Instead of solving the RTE directly, a statistical method of Monte Carlo (MC) simulation has been developed, validated, and widely accepted to model turbidity for its simple and versatile algorithms of high accuracy according to the radiative transfer theory [4,8,16,17]. The disadvantage lies in the high computational cost of the MC method to reduce variance in the results by tracking sufficiently large numbers of photons. Both the adding-doubling and MC methods have been employed as the forward model [5,10,15,17,18]. But signal measurements had to be performed with one or more integrating spheres or detector scanning to obtain signals over hemispherical or very large angular ranges, which is necessary for comparison to the calculated signals by the adding-doubling method or reducing computational time in MC simulations for a spectrophotometer. Integrating spheres are readily available as spectrophotometric accessories. Their uses, however, are limited in these instruments because of difficulties in sample assembling and signal detection in an integrating sphere. For example, the surfaces of the sample and detector holders need to be made highly reflective, 99% in reflectance, facing the inside of the sphere for accurate measurement of weak scattering signals. The highly

reflective holder surfaces and the sphere's inside surfaces require constant monitoring and maintenance for accurate determination of reflectance and transmittance from the measured signals [19]. Solving the above problems is not trivial and remains one of the barriers to development of an instrument with similar ease of use to the existing spectrophotometers.

In this report we present a spectrophotometric design and the results of system validation to determine $\mu_a(\lambda)$, $\mu_s(\lambda)$, and $g(\lambda)$ from measured signals without using an integrating sphere. Measurement of microsphere suspension samples has been performed to evaluate the accuracy, efficiency, and robustness of this approach, which adopts a fast forward model to obtain calculated signals based on an individual photon tracking MC (iMC) method accelerated through a graphic processing unit (GPU) implementation and a rapid perturbation method [11]. The high efficiency of the signal calculations enables the development of an instrument system for signal measurement using single photodiodes. The high accuracy of the modeling of the incident beam profile and detection geometry renders a robust inverse algorithm, as demonstrated by the validation results obtained with aqueous suspensions of polystyrene microspheres. We further show that critical elements of design have to be implemented in data acquisition and processing to ensure the robustness of the new instrument system.

2. METHODS

A. Experimental System

As shown in Fig. 1, a tunable light source consisting of a 175 W xenon source (XL1-175-A, WavMed Technologies Corp.) and
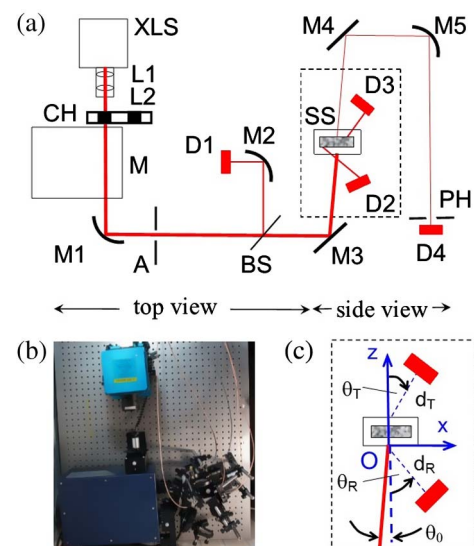
Fig. 1. (a) Schematic of the experimental setup. XLS, xenon light source; L1 and L2, lenses; CH, mechanical chopper; M, monochromator; M1 to M5, spherical or plane mirrors; A, aperture; BS, beam splitter; D1 to D4, photodiode detectors; SS, sample and holder assembly; PH, pinhole. The setup consists of two sections with the incident and measured light beams propagating either in the x–y (horizontal) plane in the top view or the x–z (vertical) plane in the side view. (b) A top-view photo of the setup, (c) the detection configuration for MC simulations of the measured signals corresponding to the part of (a) inside the dashed lines.

a monochromator (Omni-λ3005, Zolix Instruments Co., LTD) provides a nearly collimated beam with a 2 nm bandwidth and 4.6 mm × 11.0 mm cross section at the front surface of the sample holder. The beam is modulated by a chopper at frequency $f_0 = 1000$ Hz, and its power is monitored by the photodiode detector D1 as I_1. The modulated beam propagating along the x axis is then reflected into the vertical x–z plane for incidence on a sample holder in the x–y plane with an angle of θ_0 from the z axis, as depicted in the side-view section of Fig. 1.

The placement of the sample holder in the horizontal plane can effectively reduce the settling speed of the microsphere or cells in their suspensions, and thus the sample heterogeneity. The light powers are measured by three photodiode detectors: D2 for the diffusely reflected light from the sample in the holder with output signal I_2; D3 for the diffusely transmitted light with I_3; D4 for the collimated transmitted light with I_4. The incident beam has an angle from the normal of the holder's front surface of $\theta_0 = 7.0°$. The locations of the D2 and D3 detectors are determined from their distances to the front and back surfaces' centers of $d_R = 70$ mm and $d_T = 85$ mm, respectively, and orientation angles of $\theta_R = 40°$ and $\theta_T = 35°$. The geometry of detection can be accurately modeled in MC simulations, as shown in Fig. 1.

Spatial filtering is implemented with mirror M5 and pinhole PH for measurement of I_4 to reduce the contribution from the forward scatter. The photocurrent signals from the four detectors are fed to their respective channels of low-pass filtering and transimpedance amplification with adjustable gains followed by a 16-bit A/D converter (USB-AI16-16A, Access I/O Products, Inc.). The four outputs of the A/D converter are acquired by a host PC over a sampling period of 1 s at each wavelength and Fourier transformed to the extract desired signals at f_0, which are used in turn to obtain the measured signals of diffuse reflectance R_d, diffuse transmittance T_d, and the ratio of I_4/I_1 proportional to collimated transmittance T_c. The detector sensitivities and amplification gains of the four are calibrated so that the same optical power signal produces the same digital output for each channel.

B. Inverse Determination of Parameters

The forward model for obtaining calculated signals of diffuse reflectance R_{dc} and diffuse transmittance T_{dc} consists of GPU-iMC simulations and perturbation calculations. The GPU-iMC simulation solves the boundary value problems defined by the RTE and Fresnel equations. The time-independent, single-energy, and source-free form of the RTE can be written as [6]

$$\mathbf{s} \cdot \nabla L(\mathbf{r}, \mathbf{s}) = -(\mu_a + \mu_s) L(\mathbf{r}, \mathbf{s}) + \mu_s \int_{4\pi} p(\mathbf{s}, \mathbf{s}') L(\mathbf{r}, \mathbf{s}') d\omega', \quad (1)$$

where $L(\mathbf{r}, \mathbf{s})$ is the light radiance at location $\mathbf{r}$ along the direction given by the unit vector $\mathbf{s}$ and $p(\mathbf{s}, \mathbf{s}') = p(\theta, \varphi)$ can be approximated by $p_{HG}(\cos \theta)$, as discussed earlier. Figure 1 outlines the detection geometry, which has been described in detail elsewhere [11,17,20,21]. Briefly, the GPU-iMC simulation tracks individual photons in a phantom of sample holder and a turbid sample with the incident light beam represented by N_0 incident photons to accurately depict the beam's diverging angles and profile at the holder's front surface [20,21]. Signal calculations start at the first wavelength with a GPU-iMC

simulation using sample parameters initialized by the user as $\mu_{a0} = 0$, $\mu_{s0} = \mu_{t0} a_0$, and g_{s0} for a "white" reference sample. As each tracked photon enters the turbid sample inside the holder made of glass, its trajectory is followed through a sequence of scattering events until the photon hits a sample–holder interface. The Henyey–Greenstein function $p_{HG}(\cos \theta)$ is used in iMC code as the phase function. The Fresnel reflectance for unpolarized light is calculated from the local incident angle and refractive indices of the sample, and is compared to a random number (RND) uniformly distributed in [0,1] to decide if the photon reflects from or transmits through the interface. Similar treatments are performed at the holder–air interfaces. The photons exiting from the sample holder either hit one of the two detectors D2 and D3 or escape from the holder. Each photon hitting a detector is registered, and its accumulated path length within the "white" reference sample is stored as L_{so} [11]. At the completion of tracking the N_0 incident photons, the numbers of photons hitting either D2 or D3 are tallied, respectively, as N_{20} or N_{30}.

Following the GPU-iMC simulation, a perturbation method is employed to update the calculated signals of R_{dc} and T_{dc} for a simulated sample of $(\mu_{ai}, \mu_{s0}, g_0)$ by calculation of the "perturbed" number of photons hitting the D2 or D3 detector as N_2 or N_3 from N_{20} or N_{30}, respectively, with the stored tracking information L_{so} of the reference sample. With the absorption coefficient raised from $\mu_{a0} = 0$ to μ_{ai}, a total travel distance L_{ai} is obtained for each registered photon by

$$L_{ai} = -\frac{\ln(\text{RND})}{\mu_{ai}}. \quad (2)$$

If $L_{so} \geq L_{ai}$, then the registered photon is removed by updating the total hitting number as $N_i = N_{i0} - 1$, with $i = 2$ or 3; otherwise N_i remains unchanged. Upon completion of L_{ai} calculations for all registered photons, the calculated signals are derived for the simulated sample of $(\mu_{ai}, \mu_{s0}, g_0)$ as

$$R_{dc} = \frac{N_2}{N_0}, \qquad T_{dc} = \frac{N_3}{N_0}. \quad (3)$$

The perturbation calculation after a GPU-iMC simulation is iterated to obtain R_{dc} and T_{dc} from Eq. (3) for any simulated sample of (μ_a, μ_s, g) from the stored tracking records of L_{so} obtained with the reference sample of $(\mu_{a0} = 0, \mu_{s0}, g_0)$. By following the two rules detailed previously in [11], we calculate the values of R_{dc} and T_{dc} by updating L_s from L_{s0} for each registered photon. The perturbation method thus allows rapid updating of R_{dc} and T_{dc} from the initially calculated values by the GPU-iMC simulation at the first wavelength or from the values determined at the previous wavelengths.

With R_d, T_d, and μ_t as the input parameters at each λ, the calculated signals of R_{dc} and T_{dc} are obtained by either MC or perturbation methods using the initial values of albedo $a = \mu_s/\mu_t$, g, and known refractive index n for water followed by iteration [22]. Minimizing a cost function defined below guides the iteration process by variation of a and g from initial values:

$$\delta = \left(\frac{R_d - R_{dc}}{R_d}\right)^2 + \left(\frac{T_d - T_{dc}}{T_d}\right)^2. \quad (4)$$

The iteration process stops when $\delta \leq \delta_{\min}$ is achieved at each λ, with $\delta_{\min} = 0.0005$ for this study. The rule for varying a and g

is based on the relative differences between the calculated and measured signals: a is increased (or decreased) if $R_{dc} + T_{dc}$ is less (or larger) than $R_d + T_d$, while g is increased (or decreased) if R_{dc}/T_{dc} is larger (or less) than R_d/T_d. GPU-iMC simulations are performed on a personal computer with one low-cost graphics board (GT640, NVIDIA) for GPU-iMC simulations, and it takes 16–25 s to complete one simulation for tracking $N_0 = 1 \times 10^7$ photons for the results presented here. The variances of the MC calculated signals of R_{dc} and T_{dc} are found to be less than 1.0% if the solid angles of photon detection for the simulated detectors are about 0.01 (sr).

3. RESULTS

To validate the new approach, we determined the optical parameters of $\mu_a(\lambda)$, $\mu_s(\lambda)$ and $g(\lambda)$ with the diluted microsphere suspension samples from 400 to 800 nm in steps of 40 nm. A polystyrene microsphere suspension (No. 6-1-0090, Tianjin Baseline ChromTech Research Centre) was purchased for this study, which has a nominal value of weight/volume (w/v) concentration at 2.5% and a diameter d of 0.9 μm for a mean value and 10% for the coefficient of variation. The actual concentration of the purchased suspension was found to be 2.23% w/v by measurement of the suspension and microsphere masses, respectively, before and after freeze-drying of the suspension. With the corrected w/v concentration and microsphere diameter d, we determined the number concentration of the microsphere suspension to be $\rho = 1.44 \times 10^7 \,(\text{mm}^{-3})$ after a fourfold dilution in volume with distilled water for subsequent measurements. Samples were prepared by pipetting the diluted suspension into a space defined by a ring-shaped spacer with a 15.9 mm inside diameter between two glass slices that were 1.0 and 0.5 mm in thickness and examined under a microscope to ensure no formation of aggregated microspheres. The sample thickness D was determined by that of the spacer for measurement of R_d, T_d, and I_4/I_1 at each λ.

At each λ, the measured signals of diffuse reflectance $R_d = I_2/cI_1$ and diffuse transmittance $T_d = I_3/cI_1$ were acquired. The calibration factor c was determined from the ratio of light power incident on the sample holder to that measured by detector D1 as follows:

$$c = \frac{(1 - R_{BS})R_4}{R_{BS}R_3}, \qquad (5)$$

where R_{BS}, R_3, and R_4 are, respectively, the measured values of reflectance of the beam splitter and mirrors M3 and M4. The collimated transmittance T_c of a sample could be determined from I_4 and I_1, which, however, requires calibration to remove the effects of scattered light and the sample holder. Instead, we employed the ratios I_4/I_1 to determine the attenuation coefficient μ_t at each wavelength from the slope of the straight line portion of the $\ln(I_4/I_1)$ versus D curve. As shown in Fig. 2 with five samples of varying D, the contribution of the forward light scatter to $\ln(I_4/I_1)$ starts to become appreciable and dominate as D or optical thickness $\tau = \mu_t D$ increases in the case of $\lambda = 440$ nm with a large value of μ_s. For the following results, we obtained μ_t from the slope of three samples of $D = 0.318$, 0.381, and 0.504 mm, as predicted by the
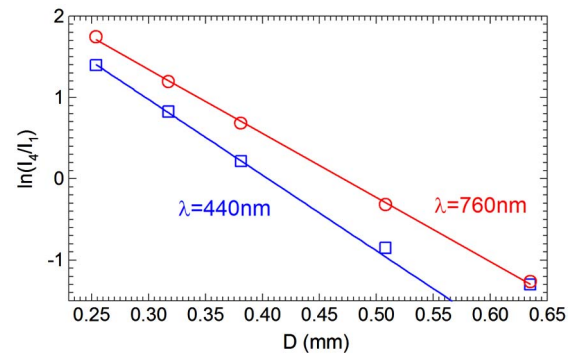
Fig. 2. Plot of the measured signals of collimated transmitted light power $\ln(I_4/I_1)$ versus the sample thickness D at two wavelengths for microsphere suspension samples. The lines are based on the Beer–Lambert law for collimated transmittance.

Beer–Lambert law, to ensure that they are on a straight line on the semi-log scale at all wavelengths.

With $\mu_t(\lambda)$, $R_d(\lambda)$, and $T_d(\lambda)$ as the input data, the scattering albedo $a(\lambda) = \mu_s(\lambda)/\mu_t(\lambda)$ and anisotropy factor $g(\lambda)$ were determined by iterating with different values of a and g to update R_{dc} and T_{dc} with the goal of minimizing the cost function δ given in Eq. (4). Most of the updates to R_{dc} and T_{dc} were carried out with the perturbation method from the stored photon tracking data by the GPU-iMC method, which took only milliseconds to complete. When a and g deviated from the values used in the previous GPU-iMC simulation by $\pm 10\%$ or more, a new simulation was performed. It has been demonstrated that the above constraint ensures the differences between R_{dc} and T_{dc} values obtained by the perturbation method and GPU-iMC simulations are less than $\pm 6\%$, which is about the same as the experimental errors of R_d and T_d [11]. Unlike the constraint on the differences between μ_s and μ_{s0} or g and g_0, perturbation-based updating of R_{dc} and T_{dc} by raising μ_a from $\mu_{a0} = 0$ is very accurate for any values of μ_a [11]. Use of the perturbation method markedly reduces the cost of forward calculations, since around 90% of the approximately 20–30 iterations per wavelength were performed by perturbation.

Figure 3 presents the optical parameters determined from the microsphere suspension samples as functions of λ. In the same figure we plot the calculated optical parameters of μ_{am}, μ_{sm}, and g_m based on the Mie code provided in [23] and the measured value of microsphere concentration ρ. Specifically, the values of the complex refractive index data of the polystyrene microspheres in [24] and real refractive index of water in [25] were used to calculate the cross sections of C_{abs}, C_{sca}, and g_m. Through microscopic examination of multiple samples of the microsphere suspension, we verified that the samples of small D values can be regarded as monodispersed without aggregated microspheres. This allows us to obtain the calculated absorption and scattering coefficients using $\mu_{am} = \rho C_{abs}$ and $\mu_{sm} = \rho C_{sca}$. Absorption by water is negligible in this spectral region [26].

The time to complete inverse determination of these parameters at 11 values of λ for each sample was determined by the total time of the GPU-iMC simulations, which took about $11 \times 3 \times 20 \text{ s} = 11$ min on average for each sample. The measured values of μ_s and g exhibit good agreement with the Mie
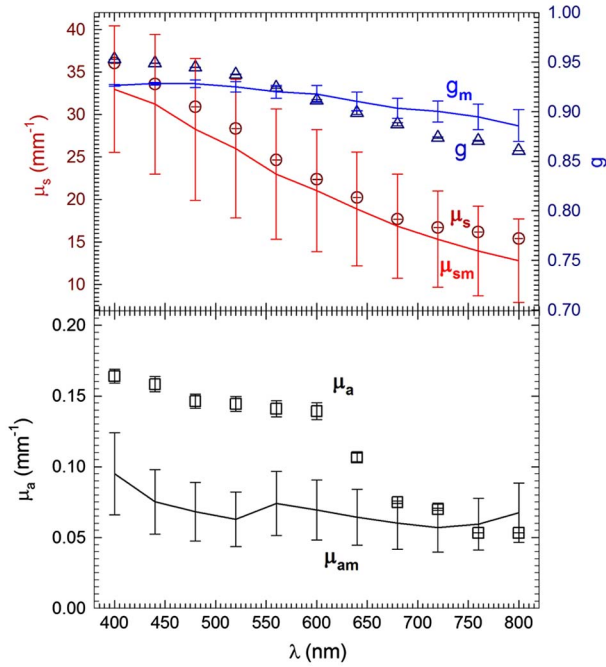
Fig. 3. Symbols and error bars are the mean values and standard deviations, respectively, of $\mu_a(\lambda), \mu_s(\lambda)$, and $g(\lambda)$ determined from three suspension samples of thickness $D = 0.318, 0.381,$ and 0.504 mm. The lines and error bars represent the calculated values of $\mu_{am}(\lambda), \mu_{sm}(\lambda)$, and $g_m(\lambda)$ by the Mie theory using the mean value of diameter $d = 0.90$ μm and its $\pm 10\%$ varied values of $d_+ = 0.99$ μm and $d_- = 0.81$ μm.

Fig. 4. Contour plots of the cost function in the parameter space of a and g for a microsphere suspension sample of $D = 0.318$ mm: (a) $\lambda = 480$ nm and (b) $\lambda = 720$ nm.

calculated values with the 10% variation of the microsphere diameters. Relatively large differences between the measured and calculated values of μ_a over the visible region of wavelength indicate a lower limit for determination of μ_a with the presented approach for samples of strong scattering with $\mu_s/\mu_a > 100$.

A robust solution for an implicit inverse problem requires not only an efficient iteration algorithm but also uniqueness guaranteed by accurate signal measurement and forward modeling for simulating signals. In an earlier study with intralipid solution samples, we initially used photodiodes of 13.0 mm^2 in the sensor area as the R_d and T_d detectors with respective solid angles for detection of scattered light of 0.00265 and 0.00180 (sr). In certain cases of longer wavelengths such as $\lambda = 720$ nm, the cost function defined in Eq. (4) could not be reduced to satisfy $\delta \leq \delta_{min}$ even by setting μ_a to 0 because R_{dc} and T_{dc} were significantly smaller than R_d and T_d. To correct the nonconverging problems, we investigated various approaches and found an effective solution by using large photodiodes of 100 mm^2 in the sensor area to increase the corresponding solid angles to 0.0204 and 0.0138 (sr). These large photodiodes were employed in the present study of microsphere suspension samples to obtain the results shown in Fig. 3.

To verify the uniqueness of the solutions for the microsphere suspension sample with the larger R_d and T_d detectors, we mapped the cost function δ in the 2D parameter space of a and g at selected wavelengths, and two examples are plotted in Fig. 4. From these results one can clearly see that the $\delta(a, g)$

functions have smooth convex forms and the corresponding optimization problems to minimize δ function well with a single minimum that can be reached from any initial location in the parameter space. In these cases, a conventional gradient descent approach suffices to yield efficient iterations [16,27].

It is interesting to examine the effects of the angular cones and the positions of the detectors on the convergence of the solutions. The need for large collection cones to detect the scattered light signals may be attributed to the deviation of the angular distribution of scattered light from the smooth function $p_{HG}(\theta)$, used as $p(\theta, \varphi)$ in our radiative transfer model. With small cones, the light signals at certain λ scattered by the sample and detected at certain angular positions could be larger than the calculated ones, even with μ_a reduced to 0. This possibility can be substantially reduced by enlarging the detection cones to obtain angularly integrated signals comparable to the calculated signals predicted with $p_{HG}(\theta)$, which can be regarded as an angularly smoothed representation of the actual phase function. The robustness is corroborated by the fact that the angular positions of the large sensors for measurement of R_d and T_d signals, θ_R and θ_D shown in Fig. 1, do not affect the results of the inverse solution (data not shown). We would like to point out that the above conclusions are correct under the condition that the two detectors are kept on the two sides of the direction of $\theta = 90°$ with a sufficiently large angular distance, 30° or larger, between them. They should also be positioned, respectively, to avoid specular reflection from the glass sample holder or the forward scatter with scattering angles less than 10°.

4. DISCUSSION

Light scattering in turbid materials is inherently anisotropic, and its angular dependence in terms of $p(\theta, \varphi)$ varies widely among different types of materials. Therefore, a "perfect" approach to analyze material turbidity would require measurement of scattered light at many angles, which is very difficult, if not impossible, to implement as an instrumentation method. In contrast, an efficient and thus practical method should take as few measured signals as possible to extract characteristic parameters and serve as common ground for quantitative comparison and classification of different materials. Such a method may not be precise but could offer a sufficiently accurate and consequently practical approach to analyze turbid materials with reasonable tolerance to errors in the measured signals.

In the approach presented here, the framework of radiative transfer theory offers much-improved accuracy over the Beer–Lambert law for quantification of turbidity, even using $p_{HG}(\cos\theta)$ to approximate the unknown scattering phase function $p(\theta, \varphi)$. While $p_{HG}(\cos\theta)$ as the scattering phase function can become erroneous in reproducing the actual angular distribution of scattered light for turbid materials, it nevertheless provides in certain cases an angularly smoothed version of the actual phase function, which may never be precisely known [28]. Moreover, $p_{HG}(\cos\theta)$ provides a rational basis for comparing different material types based on their ability to direct light scatter and considerably reduces the complexity of solving the inverse radiative transfer problems by decreasing the number of adjustable parameters. Further reduction of time to calculate signals is possible, since the speed of GPU-iMC simulations are scalable with the number of GPU cores in and performance of the graphics board. The running time of 1 min per wavelength for results shown in Fig. 3 with one nondedicated graphics board of 384 GPU cores can be readily reduced with a computer with one or multiple dedicated graphics boards of more GPU cores.

Validation results from the microsphere suspension samples demonstrate, to a certain degree, the robustness of the new approach in the determination of the three parameters $\mu_a, \mu_s,$ and g of the suspension samples, which are consistent with the literature [29–31]. The relative errors in the determination of μ_a can become large in cases where μ_s/μ_a is lager than 100. For other turbid materials, the approach should be evaluated further for its accuracy in determining $\mu_a, \mu_s,$ and g using $p_{HG}(\cos\theta)$ to approximate the unknown $p(\theta, \varphi)$. In addition, there appears to be a floor of sensitivity in determining μ_a at a level of about 0.05 (mm^{-1}) for the method described here. The major source of these limitations in the method presented relates to the measurement of the collimated transmitted signal I_4 to determine μ_t through the Beer–Lambert law, which requires samples of small optical thickness τ. As shown in Fig. 2, the portion of $\ln(I_4/I_1)$ contributed by the forward scatter becomes significant when τ exceeds 5. For samples of strong turbidity, a very small thickness D needs to be maintained, which is difficult to prepare and contributes to measurement errors in D values and the effect of air bubbles trapped inside the sample holder. Furthermore, multiple samples of varying thickness have to be measured to ensure accurate determination of μ_t from the linear slope of the $\ln(I_4/I_1)$ versus D curve. Further improvement in the measurement accuracy and efficiency could be achieved by eliminating the use of the Beer–Lambert law to determine μ_t from I_4 or T_c, which is possible with the new approach. The same GPU-iMC based forward model could be modified to calculate forward transmittance, defined as T_{fc}, which includes both the collimated transmitted light and forward scatter. The spatial filtering based on the spherical mirror M6 and pinhole PH in Fig. 1 can be easily simulated by backprojection of the collection cone of PH to the exit surface of the sample holder. The calculated signal T_{fc} can be compared to the measured signals of $T_f = I_4/cI_1$, and their squared relative difference can be added as the third term to the cost function δ in Eq. (4). These potential improvements are currently investigated, and their implementation should further relax the limits on τ and D and increase the modeling accuracy and robustness of the new spectrophotometric instruments.

5. SUMMARY

We presented a spectrophotometric design based on MC modeling to rapidly determine three optical parameters of turbid samples and their spectra without using an integrating sphere. Measurement of highly turbid microsphere suspension samples yielded results that agree with the Mie theory using an approximate phase function $p_{HG}(\cos\theta)$. This approach is the first step toward the future development of spectrophotometers for determination of turbid parameters, and additional studies need to be pursued to demonstrate the robustness of the system.

REFERENCES

1. J. G. Gibson and W. A. Evans, "Clinical studies of the blood volume. I. Clinical application of a method employing the azo dye 'Evans Blue' and the spectrophotometer," J. Clin. Invest. **16**, 301–316 (1937).
2. H. C. van de Hulst, *Multiple Light Scattering: Tables, Formulas, and Applications* (Academic, 1980).
3. R. Barer, "Spectrophotometry of clarified cell suspensions," Science **121**, 709–715 (1955).
4. V. G. Peters, D. R. Wyman, M. S. Patterson, and G. L. Frank, "Optical properties of normal and diseased human breast tissues in the visible and near infrared," Phys. Med. Biol. **35**, 1317–1334 (1990).
5. S. A. Prahl, M. J. C. van Gemert, and A. J. Welch, "Determining the optical properties of turbid media by using the adding-doubling method," Appl. Opt. **32**, 559–568 (1993).
6. V. Tuchin, *Tissue Optics: Light Scattering Methods and Instruments for Medical Diagnosis* (SPIE, 2000).
7. A. D. Klose, U. Netz, J. Beuthan, and A. H. Hielscher, "Optical tomography using the time-independent equation of radiative transfer. Part 1: Forward model," J. Quant. Spectrosc. Radiat. Transfer **72**, 691–713 (2002).
8. X. Ma, J. Q. Lu, and X. H. Hu, "Effect of surface roughness on determination of bulk tissue optical parameters," Opt. Lett. **28**, 2204–2206 (2003).
9. M. Friebel, J. Helfmann, U. Netz, and M. Meinke, "Influence of oxygen saturation on the optical scattering properties of human red blood cells in the spectral range 250 to 2000 nm," J. Biomed. Opt. **14**, 034001 (2009).
10. B. Aernouts, E. Zamora-Rojas, R. Van Beers, R. Watte, L. Wang, M. Tsuta, J. Lammertyn, and W. Saeys, "Supercontinuum laser based optical characterization of Intralipid phantoms in the 500–2250 nm range," Opt. Express **21**, 32450–32467 (2013).
11. X. Chen, Y. Feng, J. Q. Lu, X. Liang, J. Ding, Y. Du, and X. H. Hu, "Fast method for inverse determination of optical parameters from two measured signals," Opt. Lett. **38**, 2095–2097 (2013).
12. B. Aernouts, R. Watte, R. Van Beers, F. Delport, M. Merchiers, J. De Block, J. Lammertyn, and W. Saeys, "Flexible tool for simulating the bulk optical properties of polydisperse spherical particles in an absorbing host: experimental validation," Opt. Express **22**, 20223–20238 (2014).
13. R. C. Haskell, L. O. Svaasand, T.-T. Tsay, T.-C. Feng, M. S. McAdams, and B. J. Tromberg, "Boundary conditions for the diffusion equation in radiative transfer," J. Opt. Soc. Am. A **11**, 2727–2741 (1994).
14. A. P. Gibson, J. C. Hebden, and S. R. Arridge, "Recent advances in diffuse optical imaging," Phys. Med. Biol. **50**, R1–R43 (2005).
15. S. Leyre, Y. Meuret, G. Durinck, J. Hofkens, G. Deconinck, and P. Hanselaer, "Estimation of the effective phase function of bulk diffusing materials with the inverse adding-doubling method," Appl. Opt. **53**, 2117–2125 (2014).

16. Y. Du, X. H. Hu, M. Cariveau, X. Ma, G. W. Kalmus, and J. Q. Lu, "Optical properties of porcine skin dermis between 900 nm and 1500 nm," Phys. Med. Biol. **46**, 167–181 (2001).
17. C. Chen, J. Q. Lu, H. Ding, K. M. Jacobs, Y. Du, and X. H. Hu, "A primary method for determination of optical parameters of turbid samples and application to intralipid between 550 and 1630 nm," Opt. Express **14**, 7420–7435 (2006).
18. R. Watte, B. Aernouts, R. Van Beers, E. Herremans, Q. T. Ho, P. Verboven, B. Nicolai, and W. Saeys, "Modeling the propagation of light in realistic tissue structures with MMC-fpf: a meshed Monte Carlo method with free phase function," Opt. Express **23**, 17467–17486 (2015).
19. C. Chen, "Determination of optical parameters in biological tissues and application to medical imaging," Ph.D. dissertation (East Carolina University, 2008), p. 183.
20. Z. Song, K. Dong, X. H. Hu, and J. Q. Lu, "Monte Carlo simulation of converging laser beams propagating in biological materials," Appl. Opt. **38**, 2944–2949 (1999).
21. J. Q. Lu, X. H. Hu, and K. Dong, "Modeling of the rough-interface effect on a converging light beam propagating in a skin tissue phantom," Appl. Opt. **39**, 5890–5897 (2000).
22. H. Ding, J. Q. Lu, K. M. Jacobs, and X. H. Hu, "Determination of refractive indices of porcine skin tissues and intralipid at eight wavelengths between 325 and 1557 nm," J. Opt. Soc. Am. A **22**, 1151–1157 (2005).
23. C. F. Bohren and D. R. Huffman, *Absorption and Scattering of Light by Small Particles* (Wiley, 1983), p. 65.
24. X. Ma, J. Q. Lu, R. S. Brock, K. M. Jacobs, P. Yang, and X. H. Hu, "Determination of complex refractive index of polystyrene microspheres from 370 to 1610 nm," Phys. Med. Biol. **48**, 4165–4172 (2003).
25. G. Hale and M. Querry, "Optical constants of water in the 200-nm to 200-μm wavelength region," Appl. Opt. **12**, 555–563 (1973).
26. R. C. Smith and K. S. Baker, "Optical properties of the clearest natural waters (200–800 nm)," Appl. Opt. **20**, 177–184 (1981).
27. Y. Nesterov, *Introductory Lectures on Convex Optimization: A Basic Course* (Kluwer Academic, 2004).
28. J. R. Mourant, J. Boyer, A. H. Hielscher, and I. J. Bigio, "Influence of the scattering phase function on light transport measurements in turbid media performed with small source-detector separations," Opt. Lett. **21**, 546–548 (1996).
29. M. Firbank, M. Oda, and D. T. Delpy, "An improved design for a stable and reproducible phantom material for use in near-infrared spectroscopy and imaging," Phys. Med. Biol. **40**, 955–961 (1995).
30. D. Passos, J. C. Hebden, P. N. Pinto, and R. Guerra, "Tissue phantom for optical diagnostics based on a suspension of microspheres with a fractal size distribution," J. Biomed. Opt. **10**, 064036 (2005).
31. F. Bevilacqua, D. Piguet, P. Marquet, J. D. Gross, B. J. Tromberg, and C. Depeusinge, "*In vivo* local determination of tissue optical properties: applications to human brain," Appl. Opt. **38**, 4939–4950 (1999).